Project 2: Numerical Solutions to the Incompressible Navier–Stokes Equations

Aidan Green[a)]
Department of Aerospace Engineering, University of Nevada, Reno

(Dated: 24 April 2026)

The two-dimensional incompressible Navier–Stokes equations are solved numerically for the canonical lid-driven cavity problem at Reynolds numbers $Re = 100$, 400, and 1000 using a fractional-step (projection) method on a uniform staggered MAC grid. Advection is discretized with the second-order Adams–Bashforth (AB2) scheme, while viscous diffusion employs the implicit Crank–Nicolson (CN) method, yielding a stable and second-order-accurate spatial discretization. The resulting Helmholtz equations for the intermediate velocity and the pressure Poisson equation are solved via sparse LU factorization at each time step. Steady-state solutions are validated against the benchmark data of Ghia, Ghia, and Shin[?] on a 64×64 grid, demonstrating good agreement for all three Reynolds numbers. Centerline velocity profiles, streamline patterns, vorticity contours, and pressure distributions are presented, confirming the expected transition from a nearly symmetric primary vortex at low Re to a more complex recirculating structure with pronounced secondary corner eddies at $Re = 1000$.

I. INTRODUCTION

The lid-driven cavity is one of the most widely studied benchmark problems in computational fluid dynamics. Despite its simple geometry — a square domain with three stationary no-slip walls and a top wall moving at unit velocity — the resulting flow exhibits rich physical behavior, including a large primary recirculation, secondary corner vortices, and strong Reynolds-number dependence in the vortex structure and intensity. This combination of geometric simplicity and physical complexity makes the lid-driven cavity an ideal test case for verifying the accuracy and robustness of incompressible flow solvers.

A key challenge in numerically solving the incompressible Navier–Stokes equations is the enforcement of the divergence-free constraint, which couples the velocity and pressure fields through a saddle-point system. The fractional-step, or projection, method[?] addresses this by splitting the coupled system into a sequence of simpler sub-problems: an intermediate velocity field is first advanced in time ignoring the pressure, then projected onto the space of divergence-free fields via a pressure correction. This decoupling makes the method computationally efficient while retaining the accuracy of the underlying time integration scheme.

The objective of this project is to implement a fractional-step solver from scratch in MATLAB, validate the results against the high-resolution reference data of Ghia et al.[?] at $Re = 100$, 400, and 1000, and to investigate the qualitative and quantitative behavior of the flow through centerline profiles, streamlines, vorticity contours, velocity magnitude, and pressure distributions.

II. GOVERNING EQUATIONS

The dimensionless two-dimensional incompressible Navier–Stokes equations are

$$\frac{\partial \boldsymbol{q}}{\partial t} + \boldsymbol{q} \cdot \nabla \boldsymbol{q} = -\nabla p + \frac{1}{Re} \nabla^2 \boldsymbol{q}, \tag{1}$$

$$\nabla \cdot \boldsymbol{q} = 0, \tag{2}$$

where $\boldsymbol{q} = \{u, v\}^T$ is the velocity field, p is the kinematic pressure (pressure divided by density), and $Re = U_{\text{lid}} L/\nu$ is the Reynolds number defined with the lid velocity $U_{\text{lid}} = 1$, cavity side length $L = 1$, and kinematic viscosity ν.

The computational domain is the unit square $[0, 1]^2$. Boundary conditions are

$$u = 1,\ v = 0 \quad \text{(top wall, } y = 1\text{)}, \tag{3}$$

$$u = 0,\ v = 0 \quad \text{(bottom, left, and right walls)}. \tag{4}$$

Pressure satisfies homogeneous Neumann conditions on all walls, $\partial p/\partial n = 0$, with a gauge fix $p(1, 1) = 0$ to ensure uniqueness.

III. NUMERICAL METHOD

III.A. Staggered Grid Formulation

The solver employs a uniform staggered Marker-and-Cell (MAC) grid with spacing $h = 1/N$ in both directions. The horizontal velocity u is located at the centers of vertical cell faces, the vertical velocity v at the centers of horizontal cell faces, and the pressure p at cell centers. This arrangement naturally satisfies the inf-sup (LBB) stability condition and leads to a centered, second-order-accurate discrete divergence operator.

Ghost cells are used to enforce boundary conditions. For u, ghost values at the bottom and top walls are set so

that the interpolated wall velocity equals the prescribed value. Specifically, the top-wall condition $u_{\text{wall}} = 1$ is imposed via $u_{\text{ghost}} = 2 - u_{\text{int}}$, and the no-slip condition at the bottom is imposed via $u_{\text{ghost}} = -u_{\text{int}}$. Analogous expressions apply for v at the left and right walls.

The grid supports:

- u: $(N+1) \times (N+2)$ array (including ghosts), interior faces at $i = 2, \ldots, N$, $j = 2, \ldots, N+1$.
- v: $(N+2)\times(N+1)$ array (including ghosts), interior faces at $i = 2, \ldots, N+1$, $j = 2, \ldots, N$.
- p: $N \times N$ array at cell centers.

III.B. Spatial Discretization

All spatial derivatives are approximated with second-order central differences. The discrete Laplacian for u in the x-direction uses standard interior stencils, while the y-direction stencil is modified at cells adjacent to the top and bottom walls to account for the ghost-cell boundary conditions, yielding diagonal coefficients of $-3/h^2$ instead of $-2/h^2$ at these locations.

The advection operator $\mathcal{N}(\boldsymbol{q})$ is evaluated in conservative form. For the u-momentum equation:

$$\mathcal{N}_u = \frac{\partial(u^2)}{\partial x} + \frac{\partial(uv)}{\partial y}, \tag{5}$$

where fluxes are computed by averaging neighboring face velocities to the appropriate staggered locations. An analogous expression holds for $\mathcal{N}_v$.

III.C. Time Integration: Fractional-Step Method

Let $A = I/\Delta t - \nu L/2$ denote the Helmholtz operator arising from the implicit treatment of diffusion. Combining AB2 advection with CN diffusion, the semi-discrete system takes the saddle-point form[?]

$$\begin{pmatrix} A & G \\ D & 0 \end{pmatrix} \begin{pmatrix} \boldsymbol{q}^{n+1} \\ p^{n+1} \end{pmatrix} = \begin{pmatrix} \boldsymbol{r}^n + \mathrm{bc}_1 \\ 0 \end{pmatrix}, \tag{6}$$

where D and G are the discrete divergence and gradient operators, and $\boldsymbol{r}^n$ collects the Adams–Bashforth advection and explicit diffusion contributions. Applying a block LU decomposition and approximating $A^{-1} \approx \Delta t I$ yields the three-step fractional-step algorithm:

Step 1 — Intermediate velocity:

$$A\boldsymbol{q}^* = \boldsymbol{r}^n + \mathrm{bc}_1, \tag{7}$$

where the right-hand side is

$$\boldsymbol{r}^n = \boldsymbol{q}^n + \Delta t\Big(-\mathcal{N}^{n+1/2} + \frac{\nu}{2} L\boldsymbol{q}^n\Big), \tag{8}$$

and $\mathcal{N}^{n+1/2} = \frac{3}{2}\mathcal{N}^n - \frac{1}{2}\mathcal{N}^{n-1}$ is the AB2 extrapolation of the advection term.

Step 2 — Pressure Poisson equation:

$$D\,\Delta t\,G\,p^{n+1} = D\boldsymbol{q}^*. \tag{9}$$

Step 3 — Velocity correction:

$$\boldsymbol{q}^{n+1} = \boldsymbol{q}^* - \Delta t\,G p^{n+1}. \tag{10}$$

The Helmholtz system (7) is built by assembling the 2D operator via Kronecker products of 1D tridiagonal matrices with modified boundary rows, and the pressure Poisson system (9) is assembled similarly with Neumann boundary modifications. Both systems are solved using sparse LU factorization precomputed once at the beginning of the simulation, making each time step efficient.

III.D. Time Step and Stopping Criterion

The time step is selected as

$$\Delta t = \min\big(\mathrm{CFL}\cdot h,\ \ 0.25\cdot Re\cdot h^2\big), \tag{11}$$

satisfying both the advective CFL condition and the viscous stability limit. CFL values of 0.30 were used for $Re = 100$ and 400, and 0.20 for $Re = 1000$. Time integration proceeds until the steady-state criterion

$$\max\big|\boldsymbol{q}^{n+1} - \boldsymbol{q}^n\big| < \varepsilon \tag{12}$$

is met, with tolerances $\varepsilon = 10^{-7}$ for $Re = 100$ and 400, and 5×10^{-7} for $Re = 1000$.

IV. RESULTS

IV.A. Validation Against Ghia et al.

Figure 1 compares centerline velocity profiles obtained with the present solver to the reference data of Ghia, Ghia, and Shin[?] for $Re = 100$, 400, and 1000 on a 64×64 grid. The left panel shows the horizontal velocity u along the vertical centerline $x = 0.5$, and the right panel shows the vertical velocity v along the horizontal centerline $y = 0.5$.

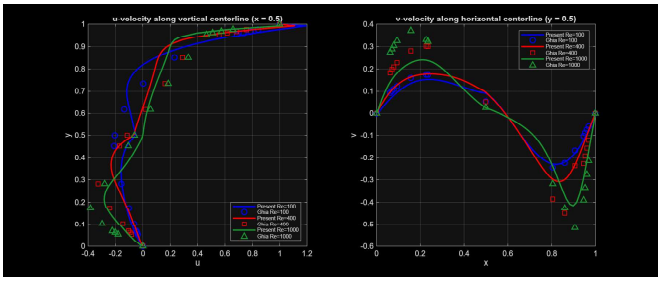

FIG. 1 Centerline velocity profiles compared against Ghia et al.[?] . *Left:* Horizontal velocity u along the vertical centerline $x = 0.5$. *Right:* Vertical velocity v along the horizontal centerline $y = 0.5$. Solid lines: present simulation; symbols: Ghia et al. benchmark data. Results are shown for $Re = 100$ (blue), 400 (red), and 1000 (green).

Agreement with the benchmark is excellent at $Re = 100$ and 400, and remains good at $Re = 1000$, where the moderate 64×64 grid begins to underresolve the thin boundary layers near the walls. At higher Reynolds numbers, the primary vortex shifts upward and toward the cavity center, while the centerline profiles develop increasingly sharp gradients — both trends captured qualitatively by the present solver.

IV.B. Streamline Topology

Figure 2 presents streamline contours at $Re = 100$, 400, and 1000. At the lowest Reynolds number, the primary recirculating vortex is nearly centered in the cavity and the flow is dominated by viscous effects. As the Reynolds number increases, inertia becomes more significant, causing the primary vortex center to migrate toward the geometric center of the cavity. Secondary counter-rotating eddies develop in the lower corners of the cavity, growing in size and intensity with increasing Re. These secondary vortices are a well-known feature of the lid-driven cavity and are consistent with the results reported by Ghia et al.

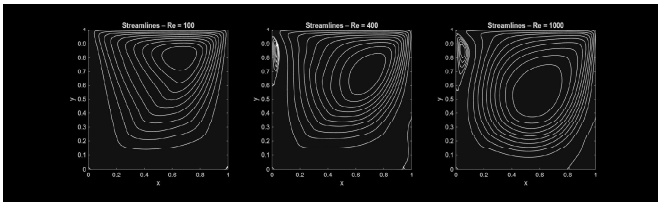

FIG. 2 Streamline contours for $Re = 100$ (left), $Re = 400$ (center), and $Re = 1000$ (right), plotted at 18 levels of the stream function ψ. White contour lines are overlaid on a dark background for clarity. The primary recirculating vortex and secondary corner eddies are visible.

IV.C. Vorticity Contours

Filled vorticity contour plots are shown in Figure 3. Positive (counter-clockwise) vorticity is generated at the moving top lid and is transported downward into the cavity interior by the primary vortex. Negative vorticity is produced at the stationary walls. At higher Reynolds numbers, the vorticity becomes increasingly concentrated in thin boundary layers along the walls, with the interior of the cavity approaching a region of near-uniform vorticity. This behavior reflects the classical boundary-layer thinning with increasing Re and is consistent with the reference results.

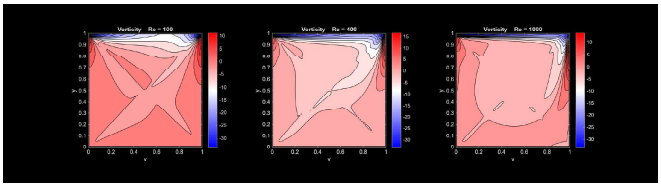

FIG. 3 Vorticity $\omega = \partial v/\partial x - \partial u/\partial y$ for $Re = 100$ (left), $Re = 400$ (center), and $Re = 1000$ (right). Blue regions indicate negative (clockwise) vorticity; red regions indicate positive (counter-clockwise) vorticity. The red-blue diverging colormap is symmetric about zero.

IV.D. Velocity Field

Figure 4 displays filled contours of velocity magnitude with superimposed velocity vectors for each Reynolds number. At $Re = 100$, the velocity magnitude is distributed relatively smoothly throughout the domain. At higher Reynolds numbers, high-speed fluid is confined to a thin region near the lid and along the side walls, while the cavity core moves more slowly. The velocity vectors clearly delineate the primary recirculation, confirming the physical plausibility of the computed flow fields.

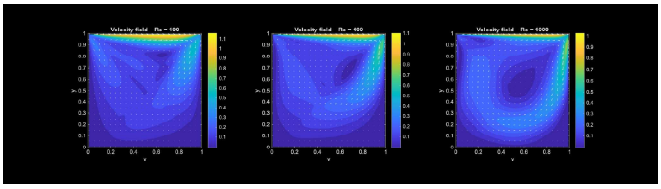

FIG. 4 Velocity magnitude contours $|\boldsymbol{q}| = \sqrt{u^2 + v^2}$ with superimposed velocity vectors for $Re = 100$ (left), $Re = 400$ (center), and $Re = 1000$ (right). Vectors are subsampled for clarity.

IV.E. Pressure Distribution

Pressure contours are shown in Figure 5. The pressure field exhibits a strong positive region in the upper-right corner of the cavity, where the lid-driven flow impinges on the right wall, and a low-pressure region in the upper-left corner. The pressure minimum near the center of the primary vortex reflects the centripetal acceleration of the recirculating fluid. As the Reynolds number increases, the pressure gradients steepen and the distribution becomes more asymmetric, consistent with the growing dominance of inertial effects.

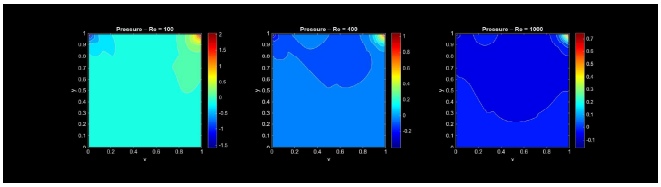

FIG. 5 Pressure field p for $Re = 100$ (left), $Re = 400$ (center), and $Re = 1000$ (right). The gauge condition $p = 0$ is enforced at the bottom-left cell center.

V. DISCUSSION

The fractional-step method implemented here successfully reproduces the benchmark results of Ghia et al.[?] across the range of Reynolds numbers tested. Several observations merit discussion.

Spatial accuracy. The staggered MAC grid with central differencing provides second-order spatial accuracy for all discrete operators. The modified diagonal entries in the Helmholtz operator near the top wall correctly account for the ghost-cell boundary conditions, ensuring consistent treatment of the lid velocity without introducing artificial forcing terms into the velocity evolution equation.

Temporal accuracy. The AB2/CN scheme is nominally second-order in time for the velocity field. However, the block-LU approximation $A^{-1} \approx \Delta t I$ used in the pressure projection introduces a splitting error of order $\mathcal{O}(\Delta t^2)$ in the divergence of the corrected velocity field. In practice, this means the pressure and velocity correction are first-order consistent, which is typical of classical projection methods of this type.

High-Re accuracy. At $Re = 1000$, the 64×64 grid is marginally sufficient to capture the primary vortex and dominant flow features, but does not fully resolve the thin boundary layers near the walls. This manifests as small discrepancies in the peak values of the centerline velocity profiles. A finer grid or a non-uniform grid with wall refinement would be needed to achieve the same level of accuracy at higher Reynolds numbers as at lower ones.

Convergence. Steady-state convergence requires significantly more time steps at higher Reynolds numbers, both because the convective time scale L/U_{lid} is approached more slowly relative to the viscous diffusion time scale, and because the solution develops more complex spatial structure that takes longer to equilibrate. The $Re = 1000$ case required up to 300 flow time units to reach the prescribed tolerance, compared to 50 for $Re = 100$.

VI. CONCLUSION

A lid-driven cavity flow solver was implemented using the fractional-step method on a staggered MAC grid, combining Adams–Bashforth advection with Crank–Nicolson diffusion. The solver was validated against the benchmark data of Ghia et al.[?] at Reynolds numbers of 100, 400, and 1000, showing good agreement in centerline velocity profiles, streamline topology, and vorticity structure. The second-order spatial discretization and ghost-cell boundary treatment were found to provide accurate results on a 64×64 grid for the moderate Reynolds numbers considered. Increasing the Reynolds number revealed the expected physics: migration of the primary vortex toward the cavity center, growth of secondary corner eddies, and thinning of boundary layers. Limitations include the use of a uniform grid, which becomes increasingly inefficient at high Re, and the first-order splitting error in the pressure projection. Future improvements could include a non-uniform grid with wall refinement, a higher-order splitting scheme, and extension to higher Reynolds numbers approaching the onset of unsteady behavior.

[a)] Electronic mail: aidangreeeen@gmail.com